

Azimuthal angular correlations between charged
 D^* mesons and hadrons in proton-proton
collisions at $\sqrt{s}=7$ TeV in ALICE

A.T. Vermeulen
Universiteit Utrecht

June 17, 2013

Abstract

The Quark Gluon Plasma (QGP) is a state of matter that is postulated in a quark model of Hadrons, Quantum Chromodynamics. The behaviour of the QGP is studied at the Large Hadron Collider in Geneva, Switzerland. Charmed mesons are used as probes for the QGP, these mesons are D mesons. In this thesis the D^{*+} meson was studied, which can be reconstructed using different subdetectors (ITS, TPC and TOF) in the ALICE experiment.

In this thesis the azimuthal angular correlations in the $\Delta\phi$ coordinates are studied. Azimuthal angular correlations are studied in order to learn more about the energy loss mechanism of the QGP, what happens to the recoil heavy quark in association with the one studied and to learn what happens to the jet fragmentation of heavy quarks modified by the interaction with the medium.

The yield and sigma for the near-side peak are extracted from the azimuthal distributions. The away-side peak is not studied because of low statistics. The yield shows the expected behaviour, where it increases with increasing transverse momentum (p_T) ranges. The behaviour of the sigma is difficult to conclude from the results. The systematic error is studied by varying the cut on the minimum number of TPC clusters.

Since this is a new study my work has mostly been contributing to the code and obtaining the first results.

Contents

1	Introduction	4
1.1	Quark Gluon Plasma	4
1.2	Heavy flavour production	4
1.3	Open charm and D meson production	4
1.3.1	The D^{*+} meson	5
1.4	Motivation for this research	5
2	Detector	7
2.1	Large Hadron Collider	7
2.2	The Alice Experiment	7
2.3	Experimental layout	7
2.3.1	Rapidity	7
2.3.2	The detector	7
2.3.3	Inner Tracking System	8
2.3.4	Time Projection Chamber	9
2.3.5	Time Of Flight Detector	9
3	Analysis	11
3.1	Data set	11
3.2	D^{*+} meson reconstruction	11
3.3	D^0 meson reconstruction	12
3.4	D^{*+} yield extraction	13
3.4.1	Invariant mass analysis	13
3.4.2	Signal extraction	14
3.5	Correction procedure for correlations	15
3.5.1	Event mixing correction	15
3.6	Efficiency correction	16
3.7	Yield extraction from the correlations	18
3.8	Extraction of systematics for single track	18
4	Results	19
4.1	D^{*+} raw yield	19
4.2	Correlation distributions	20
4.2.1	Event mixing correction	20
4.2.2	p_T integrated	21
4.2.3	Different p_T bins	22
4.3	Systematic uncertainties for single track selection	25
5	Discussion	27
5.1	Results	27
5.1.1	Mean of the fitted $\Delta\phi$ distribution	27
5.1.2	Sigma of the fitted $\Delta\phi$ distribution	27
5.1.3	Yield of the near-side peak of the fitted $\Delta\phi$ distribution	27
5.2	Missing corrections and other sources of systematic	27
5.2.1	D meson yield extraction	27
5.2.2	Fit of the $\Delta\phi$ distributions	27
5.2.3	Other sources	28

1 Introduction

1.1 Quark Gluon Plasma

The Quark Gluon Plasma (QGP) is a state of matter that is postulated in a quark model of Hadrons, Quantum Chromodynamics (QCD). The QGP is a possible state that occurs at extreme temperatures and densities, conditions comparable to just after the Big Bang. The collisions that are generated in the Large Hadron Collider at CERN are able to produce such extreme conditions.

As mentioned, the QGP is predicted in a model in which the dynamical equations are governed by the theory of QCD. QCD is the theory of the strong force and it uses color, the carrier for the strong interaction, to describe the interaction between quarks and gluons which together form hadrons.

One of the properties that arises from QCD is confinement of quarks. According to QCD, quarks are unable to be separated and only occur in the state in which they make up a hadron. The exact mechanism that causes this remains unknown. In the QGP however quarks are deconfined. This happens when the energy density of the system (~ 1 GeV/fm) or the temperature (~ 170 MeV) gets extremely high. Under these conditions a phase transition to a QGP occurs. Deconfinement of quarks only occurs within the conditions of the QGP.

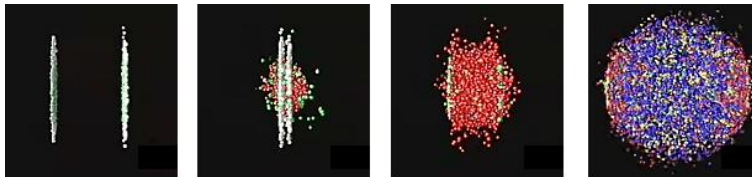


Figure 1: Formation of the Quark Gluon Plasma.

1.2 Heavy flavour production

Charm and beauty quarks are good probes of the QGP due to their short formation time compared to the lifetime of the medium. From these probes we can obtain the physical parameters that describe the QGP. At the Large Hadron Collider there are three processes that produce heavy flavour quarks:

- pair creation: $q\bar{q} \rightarrow Q\bar{Q}$ and $gg \rightarrow Q\bar{Q}$;
- flavour excitation: $qQ \rightarrow qQ$;
- gluon splitting: $q \rightarrow Q\bar{Q}$ [1].

1.3 Open charm and D meson production

As described in the section above charm is one of the heavy flavour quarks that can be used to probe the QGP. To observe a charm quark, mesons that contain them need to be detected. The studied mesons have open charm configurations, where a charm quark is bound into a meson with a light antiquark. These mesons are D mesons [1].

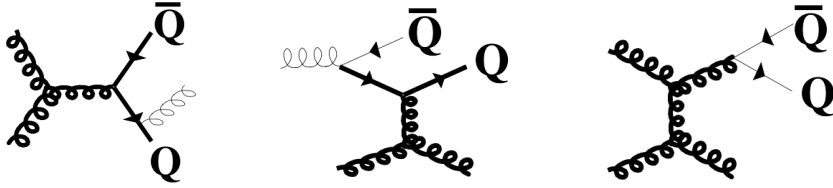


Figure 2: Feynmann diagrams of respectively pair creation, flavour excitation and gluon splitting. The thick lines are associated with hard scattering processes. Thin lines represent initial state partons or final state jets [6].

1.3.1 The D^{*+} meson

In this thesis the D^{*+} meson was studied. As a meson it consists of a quark and an antiquark, in the case of the D^{*+} it consists of a c and a \bar{d} quark. As explained in the introduction the reason that we study this meson is because it contains a charm quark.

The D^{*+} has the three decay modes: $D^{*+} \rightarrow D^0\pi_s^+$, $D^{*+} \rightarrow D^+\pi^0$ and $D^{*+} \rightarrow D^+\gamma$. We will be looking at the first decay chain $D^{*+} \rightarrow D^0\pi_s^+$ with $D^0 \rightarrow K^-\pi^+$. The D^{*+} has a branching ratio of $(67.7 \pm 0.5)\%$. The D^0 has a branching ratio of $(3.88 \pm 0.05)\%$ [8] [9].

1.4 Motivation for this research

In lead-lead collisions the QGP forms while it does not in proton-proton collisions. Proton-proton collisions are studied because a lead-lead collision is basically a superposition of protons colliding, since the lead atoms used in the Large Hadron Collider consist out of 208 protons.

When studying the QGP, the effects that the medium has on the particles, that travel through, can be quantified using the nuclear modification factor, R_{AA} :

$$R_{AA} = \frac{1}{\langle N_{bin} \rangle} \frac{d^2 N_{PbPb}(p_T)/dp_T dpy}{d^2 N_{pp}(p_T)/dp_T dpy} \quad (1)$$

When the R_{AA} is equal to one, the medium has no effect on the particles and there is no energy loss. When the R_{AA} is less than one, the medium does have an effect on the particles and there is energy loss. In figure 3 we can see, from lead-lead collisions, that the QGP has such an energy loss mechanism.

In this thesis the jet structure originating from charm quarks will be studied, using the azimuthal correlation method. The azimuthal angular correlations are studied to get a better understanding of the energy loss mechanism of the QGP. We want to know what happens to the recoil heavy quark in association with the one we study. And we want to know if the jet fragmentation of heavy quarks is modified by the interaction with the medium.

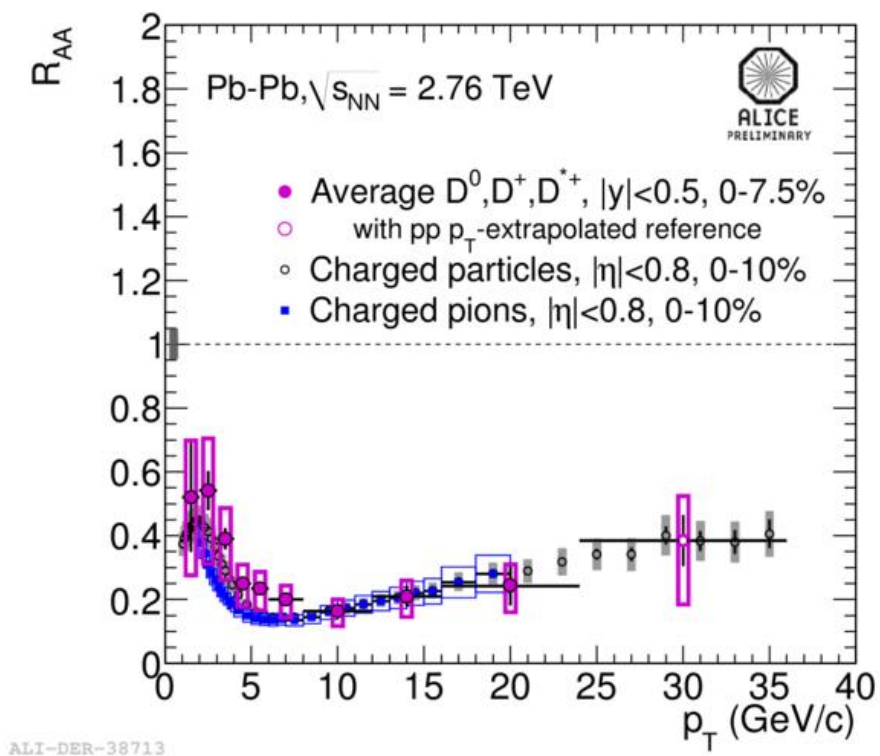


Figure 3: R_{AA} against p_T in lead-lead collisions at $\sqrt{s} = 2.76$ TeV.

2 Detector

2.1 Large Hadron Collider

The collider that delivers the data that we need in order to do the analysis is the Large Hadron Collider (LHC), the world's largest and highest-energy particle accelerator. It is built by the European Organization for Nuclear Research (CERN) and is situated in Geneva, Switzerland.

The motivation for building the LHC is to get more insight in fundamental physics questions in the field of general relativity and quantum mechanics. Several searches are worked on simultaneously, such as the Higgs boson, dark matter and in our case the QGP [2].

The collider is contained in a circular tunnel, which has a circumference of 27 kilometres. The main collider is able to accelerate protons up to 7 TeV. In order to reach this energy the particles are successively accelerated before being injected into the main collider. The particles are at first accelerated by a linear particle accelerator LINAC 2, which accelerates the protons to 50 MeV. The protons then enter the Proton Synchrotron Booster which further accelerates the protons to 1.4 GeV. Finally the Super Proton Synchrotron injects the protons into the main collider at which point the protons have an energy of 450 GeV [3].

2.2 The Alice Experiment

One of the experiments at the LHC is "A Large Ion Collider Experiment" (ALICE). The aim of this detector is to study the properties of the QGP. The detector weights 10,000 tonnes and is 26m long, 16m high and 16m wide [4]. It is one of the four main detectors at the LHC.

2.3 Experimental layout

2.3.1 Rapidity

An important element of the different detectors in the ALICE experiment is the rapidity or actually the pseudorapidity. It is defined as:

$$\eta = -\ln \left[\tan \left(\frac{\theta}{2} \right) \right] = \frac{1}{2} \ln \left(\frac{|\mathbf{p}| + p_L}{|\mathbf{p}| - p_L} \right). \quad (2)$$

The pseudorapidity depends only on the polar angle of its trajectory and not on the energy of the particle as rapidity does. We use pseudorapidity to set the range for the acceptance for the detectors. Different subdetectors consequently have different $|\eta|$ ranges, depending on their positioning. In the rest of this thesis η will be used to refer to pseudorapidity and thus detector acceptance [5].

2.3.2 The detector

The detector consists of a central detector system and a forward part. Inside the central detector system different subdetectors are mounted inside a large solenoid magnet, which generates a field of ≤ 0.5 T. The rapidity and thus the acceptance of the central detector system is $|\eta| \leq 0.9$. This will also be set as range in the analysis. The four important silicon detectors inside the central

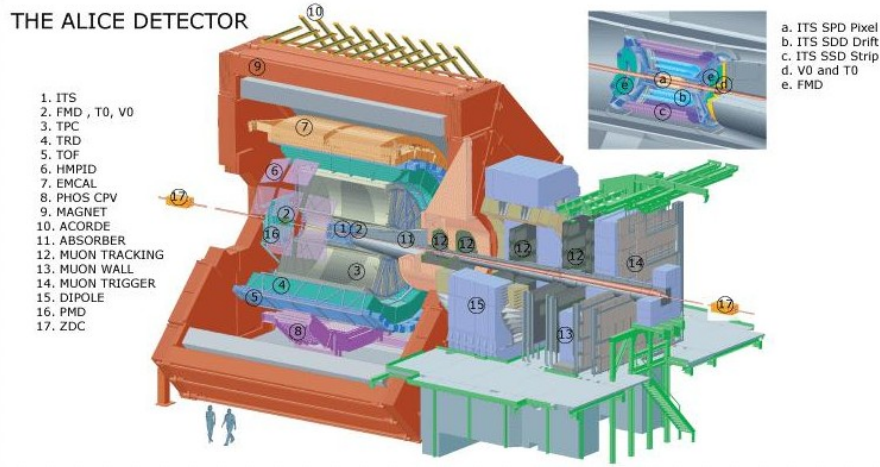


Figure 4: The ALICE detector with the layout of the different components.

system are the Inner Tracking System (ITS), Time Of Flight (TOF) and the Time Projection Chamber (TPC), these subdetectors will be explained in the following sections.

The forward part consists of four detectors. These detectors are the T0, V0, a muon spectrometer and the Forward Multiplicity Detector. The T0 and V0 detectors are used for triggering.

2.3.3 Inner Tracking System

The ITS contributes to the global tracking of the ALICE detector and has the following tasks:

- to localize the primary vertex with a resolution better than $100 \mu\text{m}$;
- to reconstruct the secondary vertices from decays of hyperons and D and B mesons;
- to track and identify particles with momentum below 100 MeV ;
- to improve the momentum and angle resolution for the high- p_t particles which also traverse the TPC;
- to reconstruct, albeit with limited momentum resolution, particles traversing dead regions of the TPC.

The ITS consists of six cylindrical layers of silicon detectors at different radii. Because the flux is much higher at a small radius (close to the beam) than at a large radius different materials are used; at smaller radii a larger resolution is needed.

SPD, SDD and SSD mean Silicon Pixel Detector, Silicon Drift Detector and Silicon Strip Detector respectively, in figure 3 [6].

Table 1: General information on the six silicon detectors of the ITS.

Layer	Type	r (cm)	$\pm z$ (cm)	Area(m^2)
1	Pixel	3.9	14.1	0.07
2	Pixel	7.6	14.1	0.14
3	Drift	15.0	22.2	0.42
4	Drift	23.9	29.7	0.89
5	Strip	37.8/38.4	43.1	2.09
6	Strip	42.8/43.4	48.9	2.68

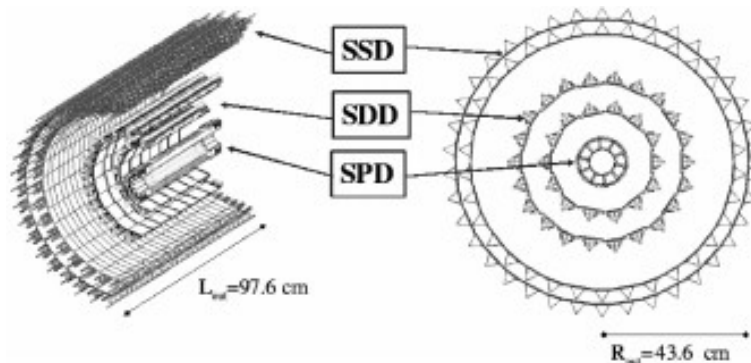


Figure 5: The layout of the ITS detectors.

2.3.4 Time Projection Chamber

The TPC is the main tracking detector in the central barrel of ALICE. The TPC is used to give spatial resolution in three dimensions, yield charge and mass mass information, and allow good pattern recognition. As a charged particle passes through the TPC, it goes through a drift chamber filled with gas. Along its trajectory it produces ion pairs. These pairs are accelerated to the end of the chamber by an electric field. From this we can determine the coordinates and energy loss of the particle.

The TPC has the following tasks:

- to measure momentum with good track separation;
- to match tracks with the other main detectors in the central barrel, the ITS and TOF;
- to measure dE/dx (energy loss) for particle identification.

The TPC consists out of the cylinders; the inner cylinder has a radius of 88cm and the outer cylinder has a radius of 250cm. The length of the cylinder is 510cm along the beam direction. The detector is filled with 88 m^3 of the drift gas Ne/CO₂ (90%/10%) [6].

2.3.5 Time Of Flight Detector

ALICE uses the Time of Flight Detector (TOF) to identify charged particles. The identification is done by the time measurement with the TOF, together with the momentum and track length measured by the other subdetectors.

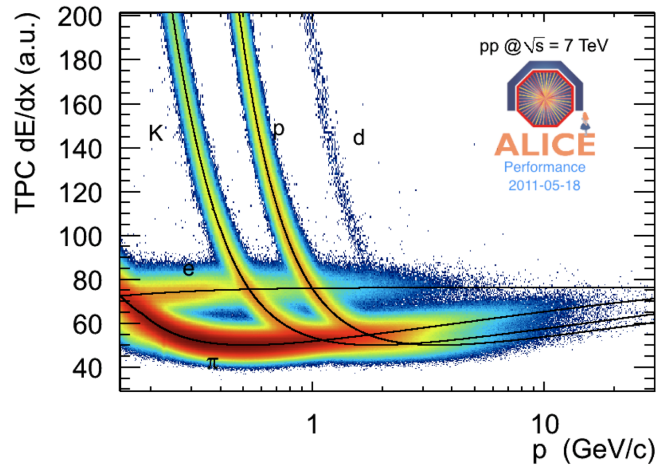


Figure 6: Particle identification using the TPC subdetector.

The TOF is triggered by the T0, a detector in the forward part. The T0 has a timing resolution of 60 ps and the TOF has a time resolution of 100 ps thus combined the total timing resolution becomes 160 ps. The TOF detector has a cylindrical shape, covering polar angles between 45 degrees and 135 degrees over the full azimuth [7].

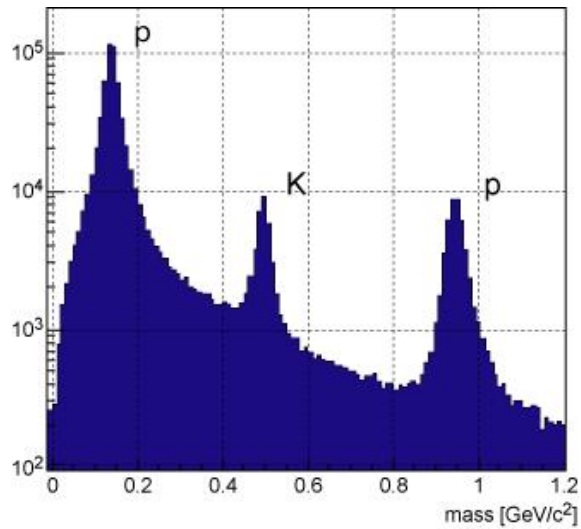


Figure 7: Particle identification using the TOF subdetector.

3 Analysis

3.1 Data set

The analysis is performed on the proton-proton at $\sqrt{s} = 7$ TeV data set taken by Alice in 2010. It contains the periods b, c, d and e. The number of runnumbers and the number of events are shown in table 2 and 3, respectively.

LHC period	Runnumber
b	117222, 117220, 117116, 117112, 117109, 117099, 117092, 117086, 117077, 117065, 117063, 117060, 117059, 117054, 117053, 117052, 117050, 117048, 116645, 116643, 116574, 116571, 116562, 116403, 116288, 116102, 115401, 115393, 115193, 115186, 114931.
c	120829, 120825, 120824, 120823, 120822, 120821, 120820, 120758, 120750, 120741, 120671, 120617, 120616, 120505, 120504, 120503, 120244, 120079, 120076, 120073, 120072, 120069, 120067, 119862, 119859, 119856, 119853, 119849, 119846, 119845, 119844, 119842, 119841, 119163, 119161, 119159.
d	126437, 126432, 126425, 126424, 126422, 126409, 126408, 126407, 126406, 126405, 126404, 126403, 126359, 126352, 126351, 126350, 126285, 126284, 126283, 126168, 126167, 126160, 126158, 126097, 126090, 126088, 126082, 126081, 126078, 126073, 126008, 126007, 126004, 125855, 125851, 125850, 125849, 125848, 125847, 125844, 125843, 125842, 125633, 125632, 125630, 125296, 125134, 125101, 125100, 125097, 125085, 125023, 124751, 122375, 122374.
e	130840, 130834, 130799, 130798, 130795, 130793, 130696, 130628, 130623, 130620, 130609, 130519, 130480, 130360, 130358, 130356, 130354, 130343, 130178, 130158, 129961, 129960, 129959, 129744, 129742, 129738, 129736, 129735, 129729, 129726, 129725, 129723, 129667, 129666, 129659, 129654, 129653, 129652, 129650, 129647, 129641, 129639, 129599, 129586, 129540, 129528, 129527, 129523, 129520, 129513, 129512, 128913, 128855, 128853, 128843, 128836, 128835, 128824, 128823, 128820, 128778, 128777, 128678, 128677, 128615, 128611, 128609, 128605, 128582, 128507, 128504, 128503, 128495, 128494, 128486, 128483, 128452, 128366, 128260, 128192, 128191, 128186, 128185, 127942, 127941, 127940, 127937, 127936, 127935, 127933, 127822, 127718, 127714, 127712.

Table 2: Runs of the proton-proton collisions taken in 2010.

LHC period	Nr. of events analysed ($\times 10^6$)
b	24.5
c	67.9
d	146.1
e	104.7

Table 3: The amount of events in the proton-proton collisions taken in 2010.

3.2 D^{*+} meson reconstruction

The reconstruction of the D^{*+} meson is done via the hadronic decay channel. This decay chain is $D^{*+} \rightarrow D^0 \pi_s^+$. Unfortunately we cannot distinguish the

primary vertex from the secondary vertex in this case, because of the decay length of the D^{*+} ($c\tau = 0.1 \mu\text{m}$).

The D^{*+} has a mass $m_{D^{*+}} = (2010.28 \pm 0.13) \text{ MeV}/c^2$. The mass of the D^0 is $m_{D^0} = (1864.86 \pm 0.13) \text{ MeV}/c^2$. Making the difference in mass $m_{D^{*+}} - m_{D^0} = (145.421 \pm 0.010) \text{ MeV}/c^2$.

From the difference in mass between the D^{*+} and the D^0 , and the mass of the pion $m_\pi = 139 \text{ MeV}/c^2$, we can conclude that the pion will have a momentum of $39 \text{ MeV}/c$ in the rest frame of the D^{*+} . Because of this we call it a soft pion π_s^+ [8] [9] [10].

In order to reconstruct D^{*+} mesons, the D^0 mesons need to be reconstructed first.

3.3 D^0 meson reconstruction

The D^0 mesons are reconstructed in the hadronic decay channel $D^0 \rightarrow K^-\pi^+$, thus combinations of the particles K^- and π^+ are being analyzed.

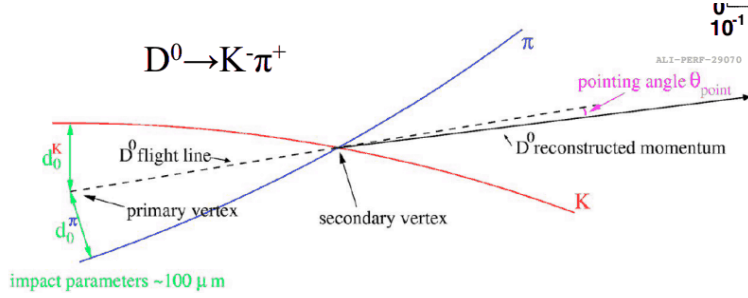


Figure 8: Topology of the D^0 meson decay.

The candidates for the D^0 meson can be found through the invariant mass [11]:

$$M(K\pi) = \sqrt{((E_K + E_\pi)^2 - (\vec{p}_K + \vec{p}_\pi)^2)}. \quad (3)$$

As a result the candidates of the D^0 meson will be obtained, but with a large combinatorial background. This combinatorial background comes from uncorrelated pairs of opposite charge that are usually contained within a jet. The following cuts are applied in order to reduce combinatorics:

- the pointing angle (angle between the reconstructed candidate and its momentum direction);
- the impact parameter of the two tracks (each separately and their product);
- the distance of closest approach;
- PID selection on the daughters.

The D^{*+} meson is then obtained by associating the D^0 candidates with a π_s^+ . The candidates of the D^{*+} meson are found through the invariant mass:

$$M(K\pi\pi) = \sqrt{((E_K + E_\pi + E_{\pi_s})^2 - (\vec{p}_K + \vec{p}_\pi + \vec{p}_{\pi_s})^2)}. \quad (4)$$

Cut Parameter	Value
ITS refit	No
TPC refit	Yes
ITS SA	No
TPC SA	No
min number of ITS clusters	0
min number of TPC clusters	70
SPD	Off
Filter bit	1
Charge	0
Associated track: p_T min	0.3 GeV/c
Associated track: p_T max	100 GeV/c
Associated track: d0 min	$-1 \cdot 10^{-9}$ cm
Associated track: d0 max	100 cm

Table 4: Cut parameters for the associated tracks.

3.4 D^{*+} yield extraction

3.4.1 Invariant mass analysis

When analysing the D^{*+} we will look at the difference between the invariant mass of the D^{*+} and the D^0 .

$$\Delta M = M(K\pi\pi) - M(K\pi). \quad (5)$$

The invariant mass in equation 5 is used because it delivers a sharper peak compared to the D^{*+} invariant mass distribution, which is given by $\Delta M = M(K\pi\pi)$. The width of the peak in this case is dominated only by the resolution of the π_s^+ tracking, instead of all three daughter particles combined. For this reason the invariant mass distribution starts at the mass of the pion, $m_\pi = 139.57 \text{ MeV}/c^2$.

The method of the selection of candidates is shown in figure 9. The selection is done within 2σ in the invariant mass of the D^0 . By taking 2σ only 95.4% of the statistics is obtained compared to 99.6% at 3σ . But in order to compute the signal the background also needs to be subtracted. It is chosen to compute the yield at 2σ because it will also take 1/3 less of the background, resulting in a smaller statistical error.

The combinatorial background of the invariant mass is estimated using the sideband method. This is done by taking the sidebands of the invariant mass of the D^0 and associating them with a soft pion candidate, to recreate a fake D^{*+} candidate.

After having obtained the combinatorial background we conclude that it is too high (see figure 10). This is explained when considered that sideband method, using the D^0 mesons, produces a larger combinatorial background compared to the signal of the D^{*+} . This is because of the shape of the invariant mass distribution of the D^0 mesons.

By calculating the ratio between the D^{*+} candidates and the sidebands, in the range $0.155 \leq M(K\pi\pi) - M(K\pi) \leq 0.175 \text{ MeV}/c^2$, the scale factor to align the combinatorial background is found to be ~ 0.8 . The scaled combinatorial background is shown in figure 11.

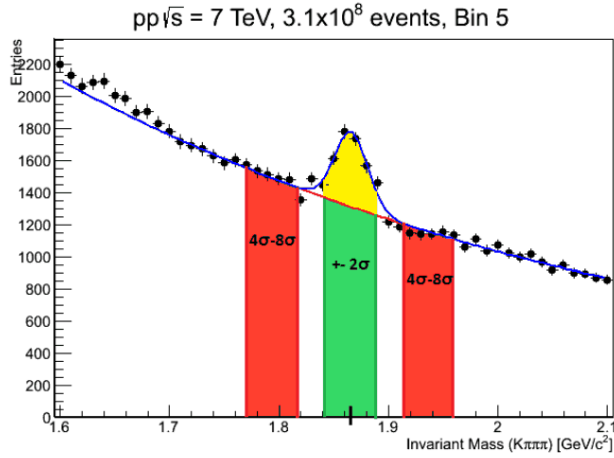


Figure 9: Invariant mass distribution of the D^0 showing the signal (yellow area) and sidebands (red areas).

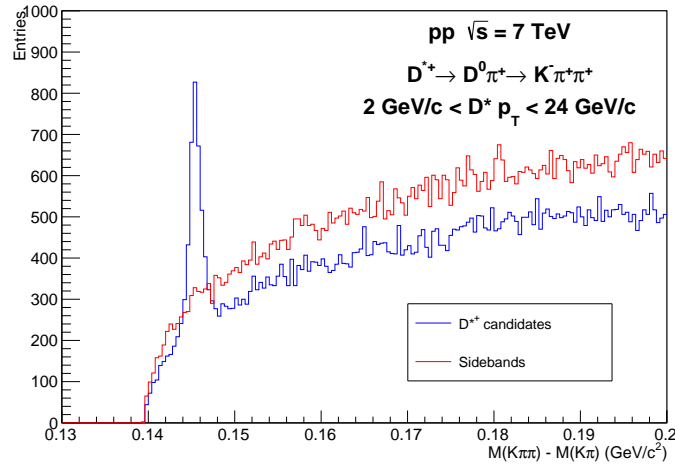


Figure 10: Invariant mass distribution ΔM showing the signal and sidebands, which are estimated too high.

3.4.2 Signal extraction

For fitting the D^{*+} candidates the background function is used with on top, a gaussian peak:

$$f_{D^{*+} \text{ candidates}}(x) = f_{\text{background}}(x) + f_{\text{gauss}}(x), \quad (6)$$

$$f_{\text{gauss}}(x) = \frac{p_0}{\sqrt{2\pi p_2^2}} e^{-\frac{(x-p_3)^2}{2p_2^2}}. \quad (7)$$

For fitting the combinatorial background the following function is used,

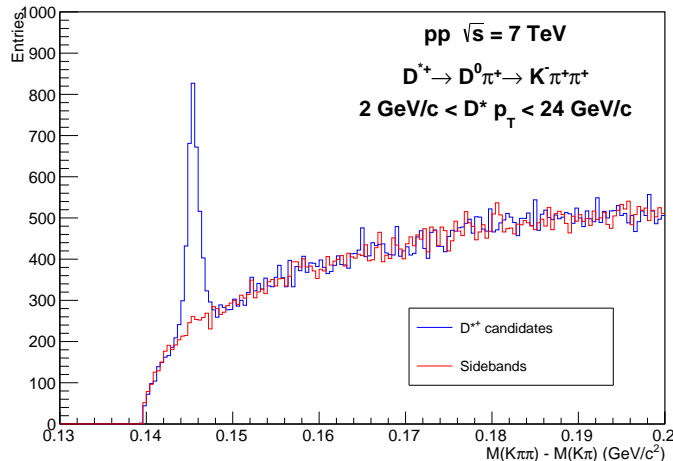


Figure 11: Invariant mass distribution ΔM showing the signal and scaled sidebands.

where m_π is the mass of the pion:

$$f_{background}(x) = p_0(x - m_\pi)^{\frac{1}{2}} e^{p_1(x - m_\pi)}. \quad (8)$$

The invariant mass distributions are fitted in the range $0.139 \text{ MeV}/c^2 \leq x \leq 165 \text{ MeV}/c^2$. From this the signal containing the number of D^{*+} mesons can be extracted, by integrating over the peak and subtracting the combinatorial background.

3.5 Correction procedure for correlations

3.5.1 Event mixing correction

The azimuthal angular correlation distributions are corrected using the event mixing technique. Mixed events are obtained by taking the D meson candidate from the event N and the associated tracks from the events. These mixed events are expected to show no physical correlations. The distribution obtained by

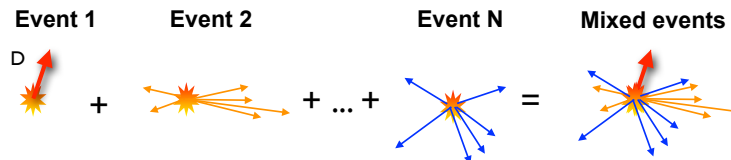


Figure 12: The method for creating mixed events.

event mixing, estimates the effects of non physical contributions to the physics we want to study, which originate from:

- the finite pseudorapidity acceptance of the detector ($|\eta| \leq 0.9$ in the ALICE case);

- the dead zones in the detector, which generates correlation shapes in the distributions we want to study.

An idealized infinite pseudorapidity acceptance will have a flat $\Delta\eta$ distribution of the particles in the event. In the case of a real detector however, we have a finite pseudorapidity acceptance. The distribution we obtain because of this will be triangular shaped. This is not a physical contribution so it is necessary to apply a correction for this.

The detector has dead zones, which are points in the detector that no longer work properly. These dead zones create holes in the azimuthal angular distributions we want to study. The correlations originating from detector inefficiencies are well reproduced by the mixed events. When we divide our single event distribution by our mixed event distribution, this effect will be corrected.

The event mixing is done online. Every processed event is stored in a event pool based on its topology. These so called pools can be intended as a sort of a matrix. The pools store events based on multiplicity and vertex position. The setup for the pools is shown table 3. All the different events contained in a pool are then mixed.

The formula applied, to correct for the mentioned effects using the obtained event mixing distribution, is as follows:

$$\frac{d^2 N^{emcorr}(\Delta\phi, \Delta\eta)}{d\phi d\eta} = \frac{\frac{d^2 N^{SE}(\Delta\phi, \Delta\eta)}{d\phi d\eta}}{\frac{d^2 N^{Mixed}(\Delta\phi, \Delta\eta)}{d\phi d\eta}} \frac{d^2 N^{mixed}(0, 0)}{d\phi d\eta}. \quad (9)$$

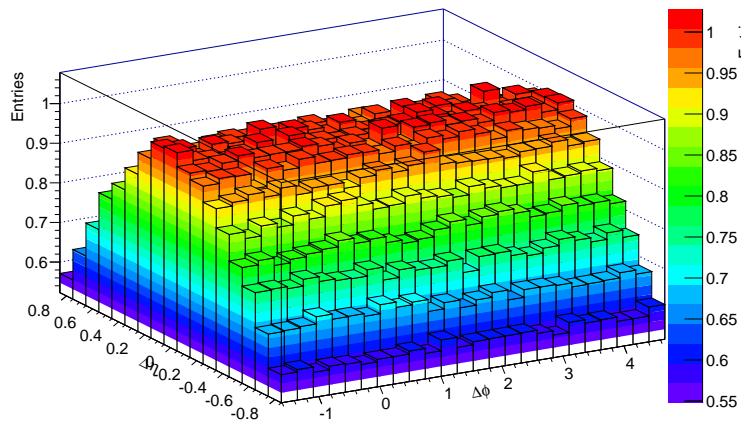


Figure 13: An example of the mixed event distributions. The triangular shape is clearly visible as well as peaks from the dead zones.

3.6 Efficiency correction

The azimuthal angular correlation distributions in $\Delta\phi$ are corrected for efficiency of the single tracks by a factor depending on the p_T bin. In figure 14 the

Event pool setting	Value
zVtx bins:	
bin 0	[-10,-2.5] cm
bin 1	[-2.5,2.5] cm
bin 2	[2.5,10] cm
Centrality (multiplicity) bins:	
bin 0	[0.0,30.0]
bin 1	[30.0,60.0]
bin 2	[60.0,1000.0]

Table 5: Used settings for the event pools.

correction factors are shown for the different p_T bins. The factor weights the correlation distribution of the associated track with 1 over this factor:

$$\frac{dN^{effcorr}}{d\phi} = \frac{dN}{d\phi} \epsilon \quad (10)$$

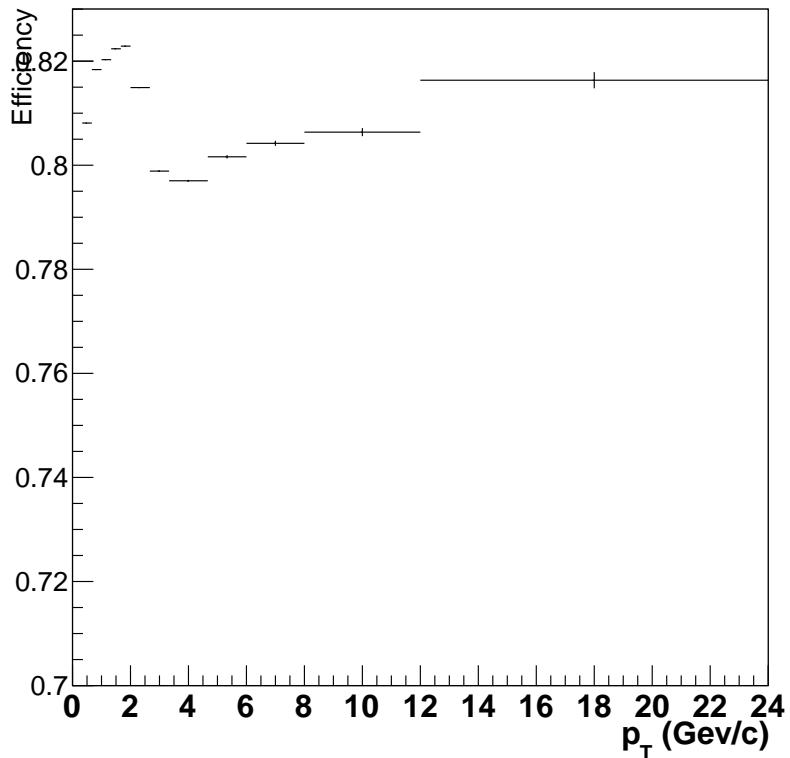


Figure 14: Single track efficiency dependence on p_T .

3.7 Yield extraction from the correlations

For fitting the $\Delta\phi$ distributions two gaussian functions are needed and a constant to account for the combinatorial background. A third gaussian, with the same parameters as the second gaussian, is added for periodicity. The following fit function is used:

$$f_{\Delta\phi}(x) = C + f_{gauss}(x, p_3 \approx 0) + f_{gauss}(x, p_3 \approx \pi) + f_{gauss}(x + 2\pi, p_3 \approx \pi) \quad (11)$$

$$f_{gauss}(x) = \frac{p_0}{\sqrt{2\pi p_2^2}} e^{-\frac{(x-p_3)^2}{2p_2^2}} \quad (12)$$

3.8 Extraction of systematics for single track

The systematic error for the yield and sigma of the $\Delta\phi$ distributions is computed by looking at different values for the cut parameter "min number of TPC clusters". Throughout this thesis the number of TPC clusters is set to 70 clusters. In order to calculate the systematic error coming from this choice, the yields and sigmas are also extracted at a minimum of 60 and 80 clusters.

By calculating the ratio between the extracted yield and sigma at 70 clusters and the extracted yield and sigma at 60 or 80 clusters the systematic error that arises is estimated.

4 Results

4.1 D^{*+} raw yield

Figure 15 represents the $\Delta M = M(K\pi\pi) - M(K\pi)$ invariant mass distribution for integrated p_T . Figures 16, 17 and 18 show the invariant mass distribution for different the p_T ranges. The p_T ranges used throughout this thesis are, [2,5], [5,8] and [8,24]. It can be seen that the sidebands allign perfect with the background of the D^{*+} candidates. The raw yields obtained from the fits of the invariant mass distributions are shown in table 4. The position and width of the gaussian peaks containing the D^{*+} candidates is shown in figure 19.

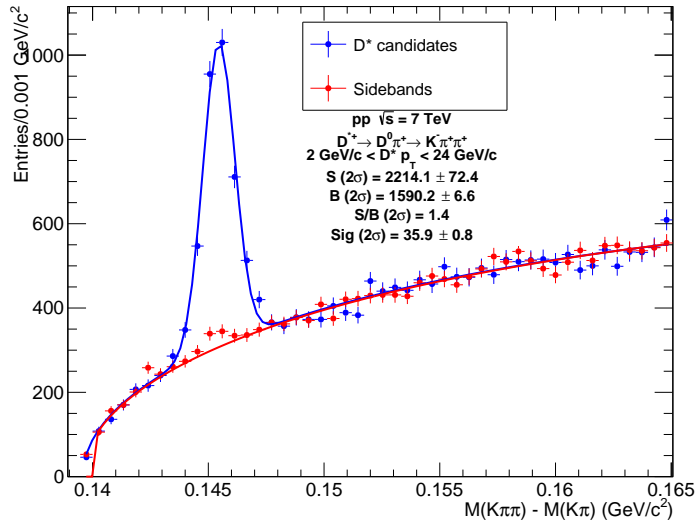


Figure 15: D^{*+} candidates p_T integrated ΔM invariant mass spectrum, where integrated over the momentum range $2 \leq p_T \leq 24$ GeV/C.

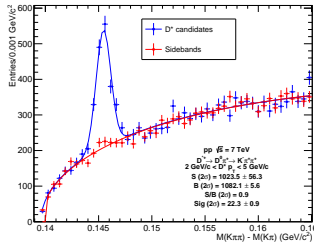


Figure 16: D^{*+} candidates ΔM , $2 < p_T < 5$ GeV/C.

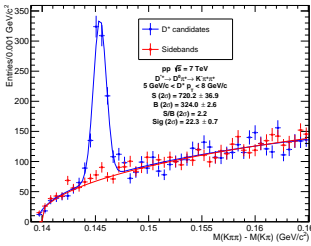


Figure 17: D^{*+} candidates ΔM , $5 < p_T < 8$ GeV/C.

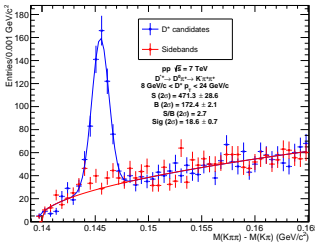


Figure 18: D^{*+} candidates ΔM , $8 < p_T < 24$ GeV/C.

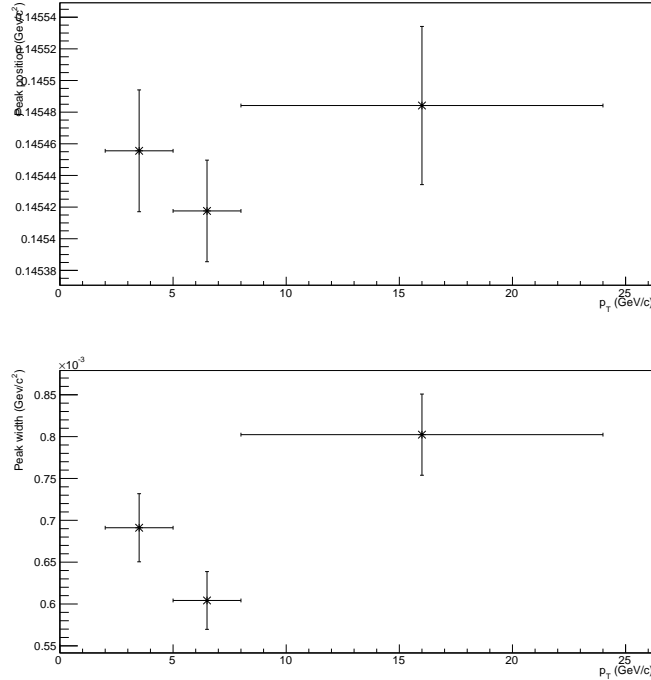


Figure 19: Fit details of the invariant mass distribution ΔM . Showing the position and width of the peak containing the D^{*+} candidates.

p_T bin [Gev/c]	Raw Yield	Significance
2,24	2214.1 ± 72.4	35.9 ± 0.8
2,5	1023.5 ± 56.3	22.3 ± 0.9
5,8	750.2 ± 36.9	22.3 ± 0.7
8,24	471.3 ± 28.6	18.6 ± 0.7

Table 6: Raw yields obtained from the fit of the invariant mass distribution ΔM at different p_T ranges.

4.2 Correlation distributions

4.2.1 Event mixing correction

First the azimuthal angular correlation distributions are corrected for non physical effects, the finite pseudorapidity and the dead zones of the detector, using event mixing. The single event distributions for the D^{*+} candidates and sideband candidates are shown in figure 20 and figure 22, respectively. The mixed event distributions for the D^{*+} candidates and sideband candidates are shown in figure 21 and figure 23, respectively. Using the correction formula (formula 9) the event mixing corrected distributions are obtained, which are shown in figure 24 and figure 25.

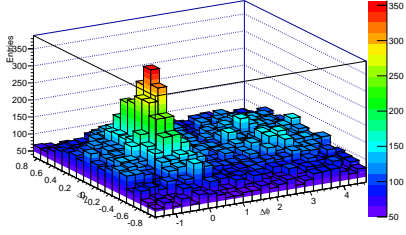


Figure 20: Single Event: D^{*+} candidates.

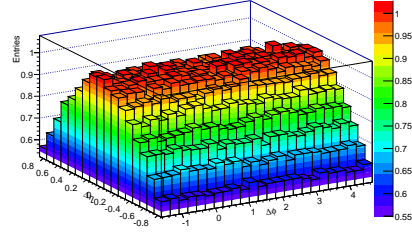


Figure 21: Mixed Event: D^{*+} candidates.

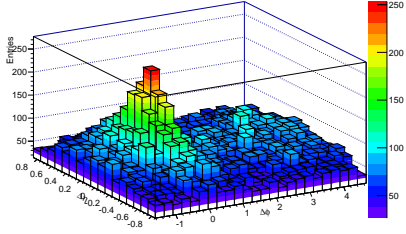


Figure 22: Single Event: Sideband candidates.

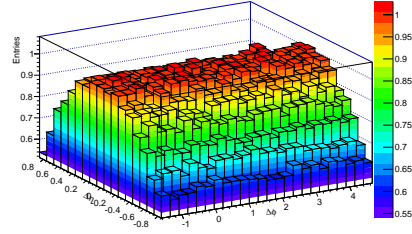


Figure 23: Mixed Event: Sideband candidates.

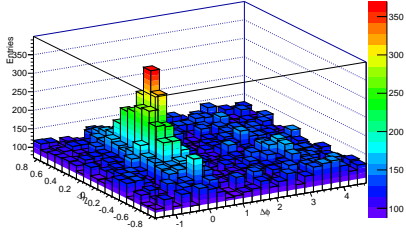


Figure 24: D^{*+} candidates after mixing correction.

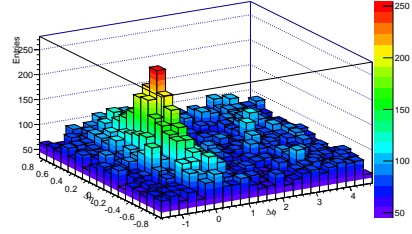


Figure 25: Sideband candidates after mixing correction.

4.2.2 p_T integrated

In figure 26 the correlations in $\Delta\phi$ are shown for the D^{*+} candidates and the sideband candidates. It shows a similar shape for D^{*+} candidates as for the sideband candidates, indicating the jet structure where the sideband candidates are reconstructed. In figure 27 the correction for the sideband candidates is applied, leaving the true correlations for the D^{*+} mesons.

For the fit the parameters of the two gaussians are set to 0 and π , for respectively the near-side and away-side peak. The only parameter that is fixed, is the constant on top of which the gaussians are fitted. The method applied to get the value for this pedestal, is by computing the average of the points that are outside of the range of the two gaussian peaks.

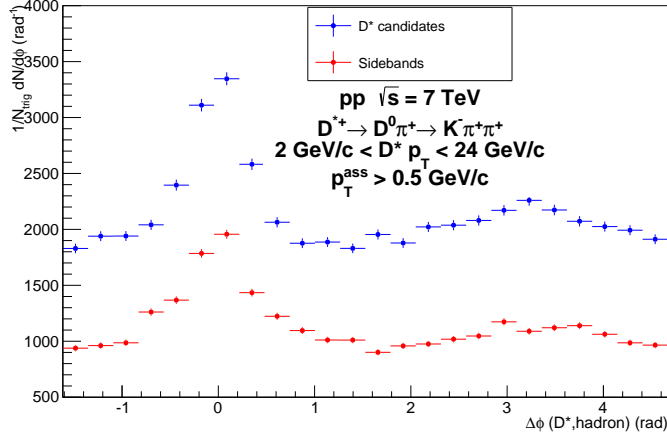


Figure 26: Correlations in $\Delta\phi$ for the D^{*+} candidates and the sideband candidates at p_T integrated.

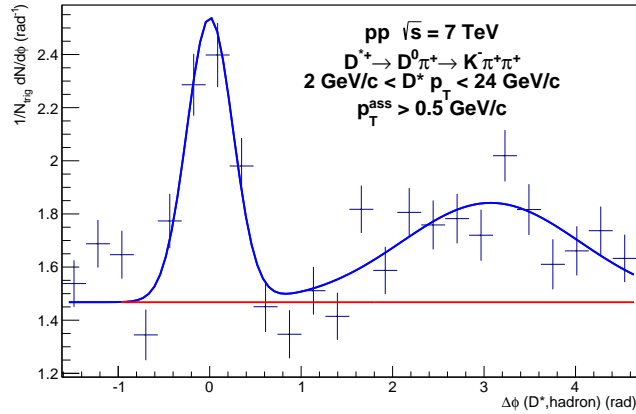


Figure 27: Corrected correlations in $\Delta\phi$.

4.2.3 Different p_T bins

The correlations $\Delta\phi$ per D^{*+} meson for different p_T bins are obtained in the same way as p_T integrated. The statistics in the away-side peak are however too low to extract meaningful parameters. For this reason the away-side peak is left unexamined. Figures 28, 29 and 30 show the obtained azimuthal angular correlations diagram for the different p_T bins. Figure 31 shows the extracted yields from the near-side peak, we can see that it increases when p_T increases. Figure 32 shows the fit details for the near-side peak. The graph on top in the figure shows the mean, which seems to be constant at zero. The graph below shows the sigma from which it is difficult to tell what trend it shows, because there are just three points.

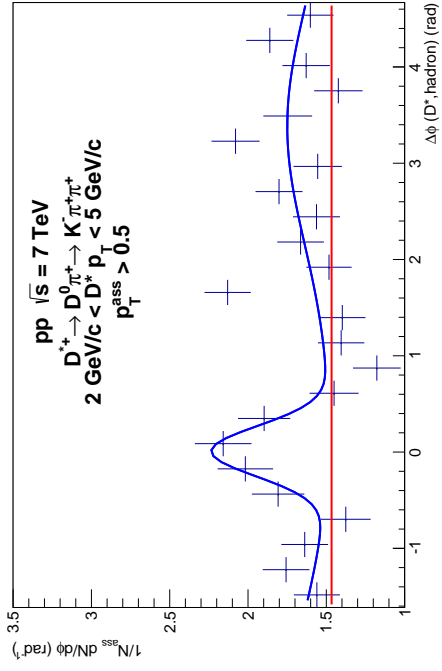


Figure 28: $\Delta\phi$, $2 < p_T < 5 \text{ GeV}/c$.

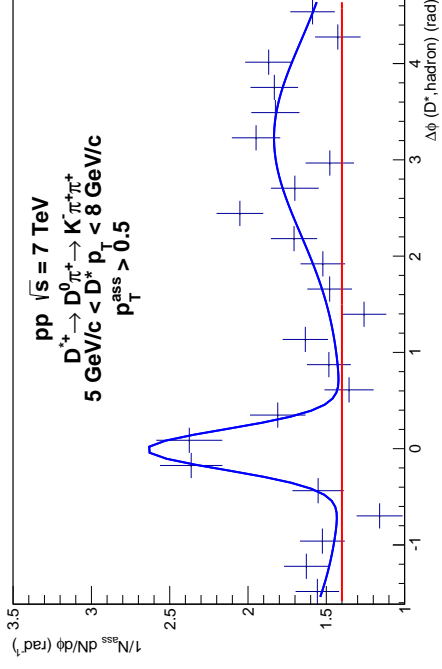


Figure 29: $\Delta\phi$, $5 < p_T < 8 \text{ GeV}/c$.

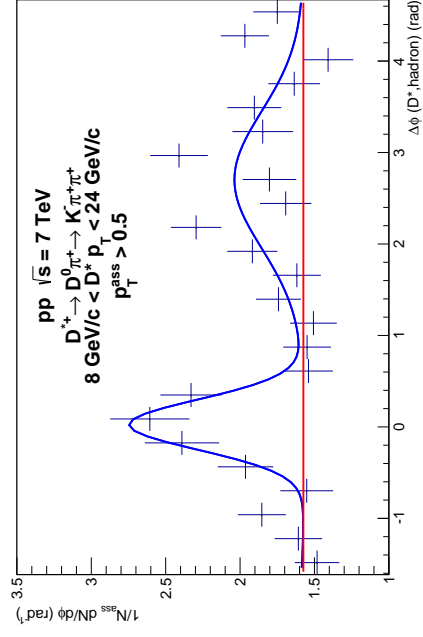


Figure 30: $\Delta\phi$, $8 < p_T < 24 \text{ GeV}/c$.

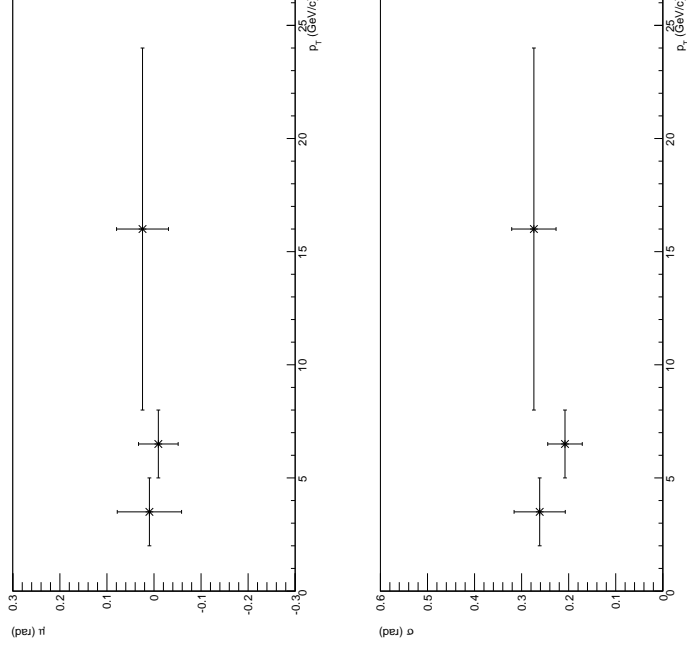


Figure 31: The extracted yield from the near-side peak for the different p_T bins.

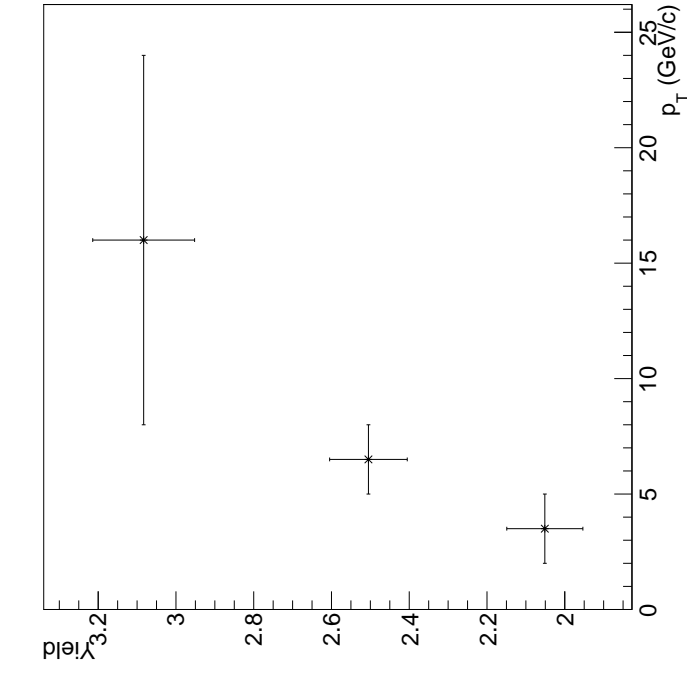


Figure 32: Fit details for the mean and sigma obtained from the $\Delta\phi$ fit for the near-side peak for the different p_T bins.

4.3 Systematic uncertainties for single track selection

The systematic uncertainty that arises in the yield extraction, by the choice of a minimum of 70 clusters in the TPC, is shown in Figure 33. The clusters chosen for comparison are a minimum number of 60 and 80 TPC clusters. The systematic uncertainties that arise in the sigma extraction is shown in figure 34. The uncertainty that arises in the yield and sigma extraction is in the range of 2%.

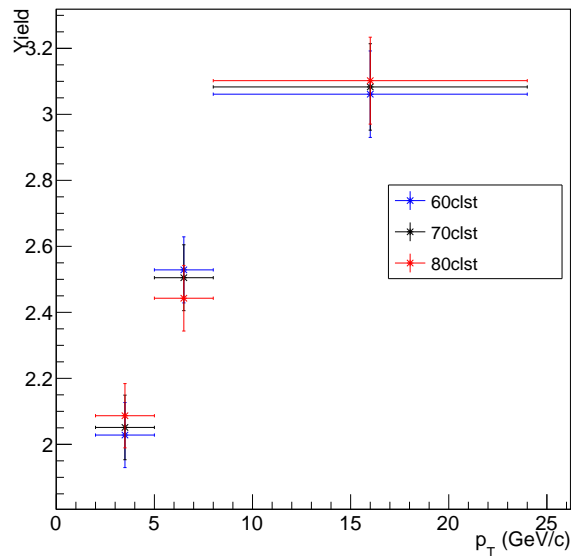


Figure 33: Extracted yields for different TPC clusters.

p_T bin [Gev/c]	Average (%)	Maximum(%)
2,5	1	2
5,8	1	3
8,24	< 1	1

Table 7: Systematics on the yield extraction per p_T bin.

p_T bin [GeV/c]	Average (%)	Maximum(%)
2,5	1	2
5,8	2	3
8,24	2	3

Table 8: Systematics on the sigma extraction per p_T bin.

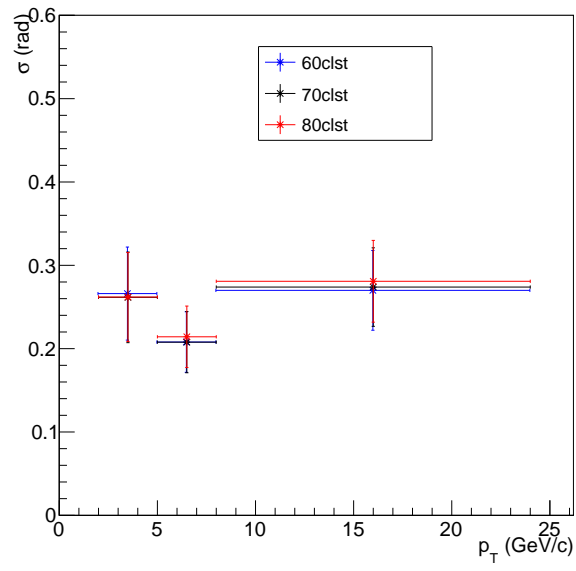


Figure 34: Extracted sigmas for different TPC clusters.

5 Discussion

5.1 Results

5.1.1 Mean of the fitted $\Delta\phi$ distribution

The mean of the near-side peak in the $\Delta\phi$ distribution is constant within errors at 0 for the different p_T bins. This is good since we expect the value of the mean to be fixed at 0.

5.1.2 Sigma of the fitted $\Delta\phi$ distribution

It is hard to determine the trend of the near-side widths, due to limited statistics available. Nevertheless one would expect a narrowing of the widths with increasing p_T , which cannot be confirmed nor ruled out at the current stage.

5.1.3 Yield of the near-side peak of the fitted $\Delta\phi$ distribution

The extracted yield from the near-side peak shows the behaviour that is expected. At higher p_T it is expected that more particles will be created, because there is more energy available for particle creation. Figure 31 shows this behaviour. Although, again, we only have three points which makes it difficult to determine the trend.

5.2 Missing corrections and other sources of systematic

5.2.1 D meson yield extraction

There are different functions that describe the combinatorial background. The one chosen in this thesis, by this choice a systematic error will arise:

$$f_{background}(x) = p_0(x - m_\pi)^{\frac{1}{2}} e^{p_1(x - m_\pi)} \quad (13)$$

But the following function also fits the combinatorial background:

$$f_{background}(x) = p_0(x - m_\pi)^{p_1} \quad (14)$$

5.2.2 Fit of the $\Delta\phi$ distributions

As described the $\Delta\phi$ distributions contain very low statistics in the away-side peak. Since we have a peak at 0 and a peak at π the maximum full width of the gaussians should be no more than $\frac{\pi}{2}$. The sigma extracted from the away-side peak exceeds this value, thus the fit for the away-side peak contaminates the fit for the near-side peak. This will give rise to a systematic error concerning the fit parameters.

Besides the method used to obtain the fit parameters, different methods for fitting the $\Delta\phi$ distribution can be used:

- a background + 2 gaussians (leave out the gaussian for periodicity);
- a background + bin counting;
- subtract the background and then fit or count the bins.

5.2.3 Other sources

Other sources of systematic can be estimated by varying the settings for the event pools used in the event mixing correction. The B-feed-down correction is not implemented yet. It should account for correlations of D^* mesons originating from a B hadron decay. At the current stage it can be done only with a MC template. The D^* meson efficiency correction is also not implemented yet. Also the contribution of secondary tracks is not taken into account.

References

- [1] Raoul Stefan de Rooij, *Prompt D^* production in proton-proton and lead-lead collisions, measured with the ALICE experiment at the CERN Large Hadron Collider*. Universiteit Utrecht, mei 2013.
- [2] <http://home.web.cern.ch/about/accelerators/large-hadron-collider>, checked on 02-06-2013
- [3] Jörg Wenninger, *Operation challenges of the LHC*. CERN Accelerators and Beams Department Operations group, november 2007.
- [4] <http://home.web.cern.ch/about/experiments/alice>, checked on 23-05-2013
- [5] Cheuck-Yin Wong, *Introduction to High-Energy Heavy-Ion Collisions*. World Scientific, ??, 1994.
- [6] The ALICE Collaboration, *Physics Performance Report, Volume 1*, J. Phys. G: Nucl. Part. Phys. 30, No 11 1517-1763, 2004.
- [7] http://aliceinfo.cern.ch/Public/en/Chapter2/Chap2_TOF.html, checked on 02-06-2013
- [8] C. Amsler et al. (Particle Data Group), $D^*(2010)^\pm$. PL B667, 1st edition, 2008.
- [9] J. Beringer et al. (Particle Data Group), D^0 . PR D86, 010001, 2012.
- [10] C. Amsler et al. (Particle Data Group), π^\pm . PL B667, 1st edition, 2008.
- [11] Ernest M Henley & Alejandro Garcia, *Subatomic Physics*. University of Washington, 3rd edition, 2007.